

A model-independent analysis of the Fermi Large Area Telescope gamma-ray data from the Milky Way dwarf galaxies and halo to constrain dark matter scenarios

M. N. Mazziotta,^{1,*} F. Loparco,^{1,2,†} F. de Palma,^{1,‡} and N. Giglietto^{1,2}

¹*Istituto Nazionale di Fisica Nucleare,
Sezione di Bari, 70126 Bari, Italy*

²*Dipartimento di Fisica “M. Merlin” dell’Università e del Politecnico di Bari,
I-70126 Bari, Italy*

(Dated: March 1, 2013)

We implemented a novel technique to perform the collective spectral analysis of sets of multiple gamma-ray point sources using the data collected by the Large Area Telescope onboard the Fermi satellite. The energy spectra of the sources are reconstructed starting from the photon counts and without assuming any spectral model for both the sources and the background. In case of faint sources, upper limits on their fluxes are evaluated with a Bayesian approach. This analysis technique is very useful when several sources with similar spectral features are studied, such as sources of gamma rays from annihilation of dark matter particles. We present the results obtained by applying this analysis to a sample of dwarf spheroidal galaxies and to the Milky Way dark matter halo. The analysis of dwarf spheroidal galaxies yields upper limits on the product of the dark matter pair annihilation cross section and the relative velocity of annihilating particles that are well below those predicted by the canonical thermal relic scenario in a mass range from a few GeV to a few tens of GeV for some annihilation channels.

PACS numbers: 95.35.+d, 98.35.Gi, 98.52.Wz, 95.75.Pq

Keywords: DM searches, dSph galaxies, Milky Way halo, Stacking analysis, Bayesian confidence intervals

I. INTRODUCTION

Milky Way dwarf spheroidal (dSph) galaxies are candidate targets for dark matter (DM) studies through annihilation signatures. This is because their mass-to-light ratio is predicted to be of the order of $10 - 10^3$ [1, 2], implying that they could be largely DM dominated. Moreover, since no significant gamma-ray emission of astrophysical origin is expected (these systems host few stars and no hot gas), the detection of a gamma-ray signal could provide a clean DM signature.

The Milky Way halo is another promising candidate for DM searches. An approach to search for DM emission from annihilation in the Galactic halo is to study the gamma-ray flux from sky positions distant from known astrophysical gamma-ray sources. The diffuse emission from unresolved sources and from the interaction of charged particles with the interstellar medium constitutes a background for this approach.

Weakly Interacting Massive Particles (WIMPs) have long been considered as well-motivated candidates for DM that could contribute to the 80% of the non-baryonic mass density in the universe [3].

At a given energy E , the differential gamma-ray flux $\Phi_\gamma(E, \Delta\Omega)$ (in units of photons $\text{cm}^{-2} \text{s}^{-1} \text{GeV}^{-1}$) from WIMP annihilation in a region covering a solid angle $\Delta\Omega$ and centered on a DM source, can be factorized as [4]:

$$\Phi_\gamma(E, \Delta\Omega) = J(\Delta\Omega) \times \Phi^{PP}(E) \quad (1)$$

where $J(\Delta\Omega)$ (in units of $\text{GeV}^2 \text{cm}^{-5} \text{sr}$) is the “*astrophysical factor*” (hereafter, *J-factor*), i.e., the line of sight (l.o.s.) integral of the DM density squared in the direction of observation over the solid angle $\Delta\Omega$:

$$J(\Delta\Omega) = \int_{\Delta\Omega} d\Omega \int_{l.o.s.} dl \rho^2(l, \Omega) \quad (2)$$

The term $\Phi^{PP}(E)$ (in units of $\text{GeV}^{-3} \text{cm}^3 \text{s}^{-1} \text{sr}^{-1}$) is the “*particle physics factor*”, that encodes the particle physics properties of the DM, and for a given WIMP mass m_χ is given by:

$$\Phi^{PP}(E) = \frac{1}{2} \frac{\langle\sigma v\rangle}{4\pi m_\chi^2} \sum_f N_f(E, m_\chi) B_f \quad (3)$$

where $\langle\sigma v\rangle$ is the WIMP pair annihilation cross section times the relative velocity of the two annihilating particles, while B_f and $N_f(E, m_\chi)$ are respectively the branching ratio and the differential photon spectrum of each pair annihilation final state f .

We note that the particle physics factor in Eq. 1 is independent of the spatial distribution of the DM, and hence independent of the particular DM source under investigation. Eq. 1 can be rewritten as:

$$\Phi^{PP}(E) = \frac{1}{J(\Delta\Omega)} \Phi_\gamma(E, \Delta\Omega) \quad (4)$$

*Electronic address: mazziotta@ba.infn.it

†Electronic address: loparco@ba.infn.it

‡Electronic address: Francesco.depalma@ba.infn.it

showing that the ratio between the photon flux and the J -factor is expected to be independent on the source if the DM annihilation mechanism is the same for all the sources. Starting from a measurement of the gamma-ray flux from a candidate DM source, if the J -factor is known, Eq. 4 allows us to obtain a measurement of the particle physics factor. If the kinematic terms of the summation in Eq. 3 are known, this measurement will yield an estimate of $\langle\sigma v\rangle$ as a function of m_χ . Moreover, since $\Phi^{PP}(E)$ is independent of the source, the results from individual sources can be combined, thus improving the measurement.

Recently two analysis approaches were developed to constrain DM models using the Fermi LAT data [5, 6]. In Ref. [5], a binned Poisson likelihood fit was used to fit both the spatial and the spectral information for the reconstructed photon events collected in a sky region around the target source. The data from 10 dSphs were also combined using a joint likelihood analysis that takes into account the uncertainties on the J -factors. The upper limits on $\langle\sigma v\rangle$ were evaluated implementing an approach based on a profile likelihood function, that incorporates the nuisance parameters. In Ref. [5] a two-year photon data sample was analyzed with the P6_V3_DIFFUSE Instrument Response Functions (IRFs) in the energy range from 200 MeV to 100 GeV. In Ref. [6] a three-year photon data sample was analyzed with the P7SOURCE_V6 IRFs in the energy range from 1 to 100 GeV. Photons from a sky region with an angular radius of 0.5° from each dSph were selected and the background was evaluated by sampling positions within an angular distance of 10° from each dSph and counting the number of events in a cone of 0.5° angular radius. The upper limits were evaluated using a fully frequentist approach that takes in account the different J -factors of each source. The authors also took the uncertainties on the J -factor into account with a semi-Bayesian approach as well. The results of these two analyses were used to set upper limits on the annihilation cross section below the canonical value for the thermal relic WIMP scenario of $3 \times 10^{-26} \text{ cm}^3 \text{ s}^{-1}$ [3, 7] up to masses of about 30 GeV for the $b\bar{b}$ and $\tau^+\tau^-$ channels. This limit could represent a serious challenge to the conventional WIMP dark matter hypothesis.

In this work we present the results obtained with a model-independent data analysis method [8] applied to DM searches. This method can be applied to the analysis of individual sources (Sect. III A) as well as to the combined analysis of multiple sources (Sect.s IIIB and IIIC), and does not introduce degrees of freedom in the calculation of confidence intervals on the parameters in the DM model. The first step of the analysis is the evaluation of upper limits on the possible gamma-ray signal events. This calculation is performed by properly choosing, for each source, a signal and a background region (see Sect.s III and IV) and following a Bayesian approach to evaluate upper limits on the signal counts. In this way no models are required

for the source and for the background. Moreover, the effects of systematic uncertainties can be easily taken into account by integrating over a nuisance parameter (either the J -factor or the effective area) the posterior probability distributions (Sect. IIID). Finally, the upper limits on the photon counts can then be converted into upper limits on $\Phi^{PP}(E)$, and consequently on $\langle\sigma v\rangle$, once a DM model has been implemented. In the present analysis we used a sample of gamma-ray data collected by the Fermi LAT during its first 3 years of operation in survey mode. The data were analyzed using the most recent LAT IRFs (P7SOURCE_V6 and P7CLEAN_V6). Candidate photons converting in both the front and back part of the instrument in the energy range from 562 MeV to 562 GeV were used for the analysis. Upper limits on $\langle\sigma v\rangle$ as a function of m_χ were obtained from the analysis of individual dSph galaxies (Sect. IV) and from their combined analysis, as well as from the analysis of the Milky Way Halo (Sect. V).

II. THE INSTRUMENT AND THE DATA

The LAT is a pair-conversion gamma-ray telescope designed to measure gamma rays in the energy range from 20 MeV to more than 300 GeV. In this paper a brief description of the LAT is given, while full details can be found in [12].

The LAT is composed of a 4×4 array of 16 identical towers designed to convert incident gamma-rays into e^+e^- pairs, and to determine their arrival directions and energies. Each tower hosts a tracker module and a calorimeter module. Each tracker module consists of 18 x-y planes of silicon-strip detectors, interleaved with tungsten converter foils, for a total on-axis thickness equivalent to 1.5 radiation lengths (r.l.). Each calorimeter module, 8.6 r.l. on-axis thick, hosts 96 CsI(Tl) crystals, hodoscopically arranged in 8 perpendicular layers. The instrument is surrounded by a segmented anti-coincidence detector that tags the majority of the charged-particle background.

A sample of gamma-ray data collected by the Fermi LAT during its first three years of operation in survey mode was used for this analysis, overlapping substantially with the data used for the second LAT source catalog [13]. The Pass7 IRFs [14] event selection cuts (for SOURCE and CLEAN event classes), with candidate photons converting in both the front and back parts of the instrument, were used. To avoid contamination from the bright limb of the Earth, data taken during any time period when the angular separation of a cone of 10° angular radius centered on the source direction with respect to the Zenith direction exceeded 105° were discarded, as well as data taken during any time period when the LAT rocked to an angle exceeding 52° . The data taken during time periods when the source was observed with an off-axis angle larger than 66.4° were also discarded.

We performed the spectral analysis using the internal LAT Collaboration software package *FermiUnfold-ing* [9–11], which enables gamma-ray spectra to be reconstructed without assuming any model for the sources or the background. The data analysis was performed selecting gamma rays with energies from 562 MeV to 562 GeV. The energy interval was divided into 12 bins, equally spaced on a logarithmic scale (4 bins per decade). We emphasize that, to take energy dispersion into account, in the unfolding approach there is a distinction between the observed photon energies and the true ones. The relationship between observed and true energy is expressed in terms of a smearing matrix, which represents the IRF and is evaluated by means of a full Monte Carlo simulation [12].

III. ANALYSIS METHODS

A. Study of individual sources

For each individual source a signal region and a background region were defined. The signal region, in which gamma rays emitted from the source are expected, was defined as a cone of a given angular radius, centered on the nominal position of the source. On the other hand, the background region was usually defined as an annulus centered on the source position and external to the signal region. To rule out possible contaminants in the background evaluation, when defining the background regions all the sources in the 2FGL catalog [13] were masked. The values of the angular radii adopted in this analysis to define the signal and background regions, as well as for masking the 2FGL catalog sources, are given in § IV and in § V.

Since the possible gamma-ray signal is expected to be faint, in each energy bin we set upper limits on the signal counts. The evaluation of the upper limits was performed following the Bayesian approach illustrated in Ref. [15]. Following the notation of Ref. [15], we indicate with n and m the number of photons detected in a given energy bin in the signal and background regions, respectively (in the following, to keep the notation simple, we will suppress the energy dependence of these variables). We assume that the probabilities of measuring the pair (n, m) are both Poissonian with expectation values $s + cb$ and b , respectively, where s is the expectation value of the signal counts (in the signal region), b is the expectation value of the background counts (in the background region) and c is defined as:

$$c = \frac{\Delta\Omega_s}{\Delta\Omega_b} \quad (5)$$

where $\Delta\Omega_{s,b}$ are the solid angles of the signal and of the background regions respectively. In principle the definition of c in the previous equation should include the livetime ratio T_s/T_b , where $T_{s,b}$ are respectively the

livetimes of the signal and of the background regions. However, since the data selection cuts illustrated in §II are performed on a cone of 10° angular radius centered on the source, and since the outer radius of the background annulus used for the present analyses is always less than 10° (see §IV), the livetime ratio T_s/T_b is always equal to 1.

The posterior probability density function (PDF) of the signal counts s was calculated assuming a uniform prior PDF for both s and b and is given by [15]:

$$p(s|n, m) = \sum_{k=0}^n a_k s^k e^{-s} \quad (6)$$

with the coefficients a_k defined as:

$$a_k = \frac{1}{\mathcal{N}} \frac{\Gamma(m+n-k+1)}{\Gamma(k+1)\Gamma(n-k+1)} \left(\frac{c}{c+1} \right)^{n-k} \quad (7)$$

where \mathcal{N} is a normalization constant.

In case of the absence of a background ($c = 0$, $m = 0$), the posterior PDF on the signal reduces to [15]:

$$p(s|n) = \frac{s^n e^{-s}}{\Gamma(n+1)}. \quad (8)$$

The upper limit on the signal counts s_u at the confidence level (or credibility level, CL) $1 - \alpha$ was evaluated by numerically solving the integral equation:

$$\int_0^{s_u} p(s|n, m) ds = 1 - \alpha. \quad (9)$$

The upper limits on the signal counts were finally converted into upper limits on the flux by means of the unfolding procedure described in [9–11]. The smearing matrix associated with each sky direction was built by taking into account the pointing history recorded by the LAT [9] and was evaluated from the Monte Carlo simulation of the LAT.

The measured upper limits on the flux were then converted into upper limits on $\langle\sigma v\rangle$. From Eqs. 3 and 4 it follows that:

$$\langle\sigma v\rangle = \frac{1}{J(\Delta\Omega)} \Phi_\gamma(E, \Delta\Omega) \times \frac{8\pi m_\chi^2}{\sum_f B_f N_f(E, m_\chi)}. \quad (10)$$

For each value of m_χ the conversion of the limits on the gamma-ray flux into limits on $\langle\sigma v\rangle$ was performed by requiring that the flux predicted from the model must not exceed the measured photon flux in any energy bin. The expected gamma-ray flux from the DM annihilation channels was evaluated as a function of energy using the DMFIT package [16] based on DarkSUSY [17], as implemented in the LAT Science Tools [18]. For large

DM masses (around or above 1 TeV), the radiation of soft electroweak bosons leads to additional gamma rays in the energy range of relevance for the present analysis (see e.g. [19, 20]). This emission mechanism is not included in the DMFIT package. Therefore the present analysis provides conservative upper limits on $\langle\sigma v\rangle$.

B. Stacking analysis

According to Eq. 4, the particle physics factor is independent of the source under investigation. This feature suggests the possibility of combining the data from all individual sources in order to improve the constraints on the DM models.

Once the individual sky directions were analyzed, a stacking analysis was performed. In this case the counts from the signal and background regions corresponding to each source were added, and the upper limits on the signal were evaluated following the same procedure as for individual sources.

In order to implement the same analysis procedure as for individual sources, in the stacking analysis the ratio between the signal and background regions was defined as:

$$c = \frac{\sum_i \Delta\Omega_{si} T_{si}}{\sum_i \Delta\Omega_{bi} T_{bi}} \quad (11)$$

where $\Delta\Omega_{si,bi}$ and $T_{si,bi}$ are respectively the solid angles and the livetimes of the signal and background regions of the i -th source ($T_{si} = T_{bi}$ according to the discussion in §III A).

We note that a more detailed statistical analysis (see the discussion in Appendix A) shows that the coefficient c should be defined as:

$$c = \frac{\sum_i c_i (m_i + 1)}{\sum_i (m_i + 1)} \quad (12)$$

where c_i is the coefficient defined in Eq. 5 for the i -th source and m_i are the counts in the background region of the i -th source.

If the coefficient c is defined as in Eq. 11, its value will depend only on the extensions (solid angles) of the signal and background regions and on the livetimes of the stacked sources. On the other hand, if c is defined as in Eq. 12, its value will also depend on the data (counts in the individual background regions). In the stacking analysis of the dSph galaxies we evaluated the coefficients c using both the definitions in Eq. 11 and Eq. 12. We found that the differences in the values of c obtained implementing the two different definitions were negligible in all the energy bins.

The different exposures of the individual sources were also taken into account in the evaluation of the smearing matrix [9], which was performed by stacking the pointing histories of all the sources. This procedure is equivalent

to stacking the events from each sky direction on top of one another and then analyzing the resulting image (as an example see the last panels in Figs. 2 and 3 for the case of the dSph analysis).

Since the sources may be seen by the instrument with different exposures, the J -factor value used in the stacking analysis was defined as the average of the J -factors of individual sources, each one weighted with its exposure in the whole energy interval under investigation. In principle, different J -factors should be determined for each energy bin, with each one evaluated taking into account the exposures in the corresponding bin. We performed this calculation in the case of the dSph galaxies, and the differences between the J -factors evaluated using the exposures in individual energy bins with respect to the J -factor evaluated using the overall exposure were less than 1%. Since these differences are small, we decided to use the same J -factor for the whole energy interval, evaluated using the overall exposure. In this way we also avoided introducing an energy dependence of the J -factor that may seem unphysical since, according to Eq. 2, the J -factor is determined only by the DM density profile.

The upper limits on $\langle\sigma v\rangle$ were evaluated in the same way as for individual sources.

C. Composite analysis

In the previous analysis the events from all the sources were stacked. This is equivalent to considering the set of all the sources as a single source with a J -factor given by the average value weighted with the exposures of all the sources. In the stacking method all the sources are treated in the same way, and photons from a source with a small J -factor are considered as likely to originate from DM as photons from a source with a large J -factor. However, in the absence of a clear gamma-ray signal, i.e., if the counts in the signal region n are compatible with the expected background ($n \approx c m$), a source with a higher J -factor will yield a lower upper limit with respect to a source with a lower J -factor. The “DM sensitivity” of each source is therefore determined by its J -factor.

To account for the different sensitivities of each observation we developed a composite analysis approach that combines the results from all the sources taking into account the individual J -factors. Unlike the approaches discussed in sections III A and III B, for simplicity, in this approach we do not treat the energy resolution. Since the 68% containment of the energy resolution of the LAT in the energy range chosen for the present analysis is less than 15% [14], we expect that neglecting the energy dispersion in the evaluation of the flux could yield a similar uncertainty. Indeed we verified, in the case of dSph galaxies, that the differences between the fluxes reconstructed either neglecting or taking into account the energy dispersion are of the order of a few percent in the whole energy range of the analysis.

Indicating with s_i the expected signal counts from the i -th source in the energy interval $[E, E + \Delta E]$ (again, for simplicity, we will suppress the energy dependence of these variables), it is possible to define the random variable u as:

$$u = \eta_i s_i \quad (13)$$

with the factor η_i defined as:

$$\eta_i = \frac{1}{J_i \mathcal{E}_i(E) \Delta E} \quad (14)$$

where J_i is the J -factor of the i -th source and $\mathcal{E}_i(E)$ is its exposure in the energy bin $[E, E + \Delta E]$, which is given by:

$$\mathcal{E}_i(E) = \int dt f_{LT}(t) A_i(E, t) \quad (15)$$

where $A_i(E, t)$ is the effective area and $f_{LT}(t)$ is the livetime fraction. The dependence on t in Eq. 15 indicates that the aspect angles (off-axis and azimuthal angles in the instrument frame) corresponding to the given sky direction (source) are changing with time.

Since u is equal to $(1/J)\Phi_\gamma(E, \Delta\Omega)$, and hence to $\Phi^{PP}(E)$, it is independent of the particular source under investigation.

A set of PDFs for the random variable u can be evaluated starting from the data of each source. Indicating with n_i and m_i the counts in the signal and background regions of the i -th source, the PDF for s_i is given by Eq. 6, which can be rewritten explicitly indicating the source index as:

$$p_i(s_i | n_i, m_i) = \sum_{k=0}^{n_i} a_{ik} s_i^k e^{-s_i} \quad (16)$$

with the coefficients a_{ik} defined as in Eq. 7.

The i -th PDF for the variable u can be derived from Eq. 16, and is given by:

$$p_i(u | n_i, m_i) = e^{-u/\eta_i} \sum_{k=0}^{n_i} b_{ik} u^k \quad (17)$$

with the coefficients b_{ik} defined as:

$$b_{ik} = \frac{a_{ik}}{\eta_i^{k+1}}. \quad (18)$$

To combine a set of N sources we build the likelihood function:

$$\mathcal{L}(u | n_1, m_1; n_2, m_2; \dots; n_N, m_N) = \prod_{i=1}^N p_i(u | n_i, m_i). \quad (19)$$

Expanding the calculations in the previous equation, the final expression of the likelihood function is given by:

$$\mathcal{L}(u) = e^{-u/\eta} \sum_{k=0}^{n_{max}} f_k u^k \quad (20)$$

where η and the set of coefficients f_k are defined as follows:

$$1/\eta = \sum_{i=1}^N \frac{1}{\eta_i} \quad (21)$$

$$f_k = \sum_{\substack{k_1, k_2, \dots, k_N \\ k_1 + k_2 + \dots + k_N = k}} \prod_{i=1}^N b_{ik_i}. \quad (22)$$

In the summation of Eq. 20 the maximum value of k yielding a non-zero coefficient f_k is $n_{max} = n_1 + n_2 + \dots + n_N$.

In case of the absence of a background the expression of the likelihood function becomes simpler. Starting from Eq. 8, it is straightforward to show that the expression of the likelihood function is given by:

$$\mathcal{L}(u) = e^{-u/\eta} u^n \prod_{i=1}^N \frac{1}{\eta_i^{n_i+1} \Gamma(n_i+1)} \quad (23)$$

where

$$n = \sum_{i=1}^N n_i. \quad (24)$$

The likelihood function obtained from Eq. 20 (or Eq. 23) is not normalized because, having assumed that $u = s_i/\eta_i$ is independent of the source under investigation, the measurements (n_i, m_i) are not independent of each other. To ensure normalization, the function $\mathcal{L}(u)$ must be multiplied by a constant \mathcal{A} , which in the general case of Eq. 20 is given by:

$$\mathcal{A} = \frac{1}{\sum_{k=0}^{n_{max}} \frac{f_k \Gamma(k+1)}{\eta^{k+1}}}. \quad (25)$$

Once the likelihood function is normalized, the upper limit u^* at the CL $1 - \alpha$ can be evaluated by numerically solving the equation:

$$\int_0^{u^*} \mathcal{A} \mathcal{L}(u) du = 1 - \alpha. \quad (26)$$

D. Systematic uncertainties

Systematic uncertainties on the J -factor as well as on the effective area can be taken into account in the above procedures introducing a nuisance parameter in the definition of the random variable u . In the following we will illustrate the calculations to take into account the systematic uncertainties on the J -factors; the mathematical formalism used in the calculations to take into account systematic uncertainties on the effective area is similar so we do not present it here.

Similar to the approach in §III C, it is possible to define the random variable u as:

$$u = \rho_i \frac{s_i}{J_i} \quad (27)$$

where the factor ρ_i is defined as:

$$\rho_i = \frac{1}{\mathcal{E}_i(E)\Delta E}. \quad (28)$$

Unlike in §III C, in this case the dependence of u on J_i is written explicitly in order to take fluctuations in J_i into account.

The posterior PDF for u can be obtained starting from the joint PDF $p_i(s_i, J_i)$ for s_i and J_i as:

$$p_i(u) = \frac{1}{\rho_i} \int J_i p_i(J_i u / \rho_i, J_i) dJ_i. \quad (29)$$

Since s_i and J_i are independent random variables, their joint PDF can be factorized, and the previous equation rewritten as:

$$p_i(u) = \frac{1}{\rho_i} \int J_i p_i(J_i u / \rho_i) p_i(J_i) dJ_i. \quad (30)$$

where the PDF $p_i(s_i)$ is given by Eq. 16.

To make the calculation simpler, for the J -factors a uniform PDF in the range $[J_{i1}, J_{i2}]$ is assumed, i.e. $p_i(J_i) = 1/\Delta J_i$. Introducing these PDFs in the previous equation, the posterior PDF for u is given by:

$$p_i(u) = \frac{1}{\rho_i \Delta J_i} \sum_{k=0}^n a_k \int_{J_{i1}}^{J_{i2}} J \left(\frac{uJ}{\rho_i} \right)^k e^{-uJ/\rho_i} dJ. \quad (31)$$

The upper limit u^* at the CL $1 - \alpha$ is evaluated by numerically solving the integral equation:

$$\int_0^{u^*} p_i(u) du = 1 - \alpha \quad (32)$$

where $p_i(u)$ is given by Eq. 31.

A similar approach is implemented to evaluate the effects of the systematic uncertainties on the effective

area of the instrument. In this case the effective area is treated as a uniformly distributed random variable, while the J -factor is assumed to be known.

For the stacking analysis, the same procedure was implemented as for the analysis of individual sources. In this case the PDF for u was obtained starting from the cumulative signal and background counts, as in §III B.

In the case of the composite analysis, the likelihood function was built by multiplying all the individual PDFs $p_i(u)$ in Eq. 31, and then the upper limits on u were evaluated as discussed in §III C.

IV. ANALYSIS OF THE DWARF SPHEROIDAL GALAXIES

This analysis was performed using P7SOURCE_V6 class events. For each source, events within a cone of 10° angular radius centered on the nominal position of the source were selected. Again we note that, because of the selection cuts described in §II, all sky directions within 10° from the source will have the same live time.

The positions of the dSph galaxies considered in the present analysis and the corresponding values of their J -factors are reported in Tab. I, which is taken from Ref. [5]. These dSph galaxies are not included in the second catalog of the Fermi LAT [13], i.e., they are not detected in the gamma-ray energy band above 100 MeV. In our analysis we assumed that the J -factor distribution for each dSph is well described by a log-normal function (see Ref. [5] for more details), with average value and standard deviation of $\log_{10} J$ reported in Tab. I. The half-light radii of the dSph galaxies used to compute the J -factors are less than or close to 0.5° . The average values $\langle J_i \rangle$ were calculated from the log-normal distributions as:

$$\langle J_i \rangle = \exp \left(\mu_i + \frac{1}{2} \sigma_i^2 \right) \quad (33)$$

where μ_i and σ_i^2 are the average value and the variance of the distributions of $\ln J_i$, which can be calculated multiplying the values reported in Tab. I by $\ln 10$.

When evaluating the effects of systematic uncertainties on the J -factor, we followed the procedure discussed in §III D. The fluctuations of J_i were described by a uniform PDF in the interval $[J_{i1}, J_{i2}]$, with J_{i1} and J_{i2} corresponding to the 16% and 84% quantiles of the log-normal distribution.

In the case of the stacking analysis, as discussed in §III B, the J -factor was evaluated as the weighted average of the J -factors of individual dSph galaxies with the exposures. The distribution of the J -factors of the stacked sources was built sampling a large set of events (10^6) from the J -factor distributions of individual sources, and is shown in Fig. 1. The average value of the J -factor for the stacked sources is $\langle J \rangle = 1.75 \cdot 10^{19} \text{ GeV}^2 \text{ cm}^{-5} \text{ sr}$. As in the case of individual sources, to study the systematic uncertainties

Name	Galactic longitude	Galactic latitude	$\log_{10}(J)$ ($\text{GeV}^2\text{cm}^{-5}\text{sr}$)
Bootes I	358.08°	69.62°	17.7 ± 0.34
Carina	260.11°	-22.2°	18.0 ± 0.13
Coma Berenices	241.9°	83.6°	19.0 ± 0.37
Draco	86.37°	34.72°	18.8 ± 0.13
Fornax	237.10°	-65.7°	17.7 ± 0.23
Sculptor	287.15°	-83.16°	18.4 ± 0.13
Segue I	220.48°	50.42°	19.6 ± 0.53
Sextans	243.4°	42.2°	17.8 ± 0.23
Ursa Major II	152.46°	37.44°	19.6 ± 0.40
Ursa Minor	104.95°	44.80°	18.5 ± 0.18

TABLE I: List of the dSph galaxies used in this analysis. The J -factors are assumed to be distributed according to a log-normal distribution with $\langle \log_{10} J \rangle$ and $\sigma_{\log_{10} J}$ given here. The half-light radii of the dSph galaxies used to compute the J -factors are less than or close to 0.5° [5].

on J we used a uniform PDF in the interval $[J_1, J_2]$, with J_1 and J_2 corresponding to the 16% and 84% quantiles of the resulting J -factor distribution.

For each dSph galaxy the signal region was defined as a cone of angular radius $\Delta\theta = 0.5^\circ$ centered on the source position. The value of $\Delta\theta$ is the same as the one used to evaluate the J -factor, and is consistent with the Point Spread Function (PSF) of the instrument, the 68% containment radius of which is smaller than 1° in the energy range above 1 GeV [14]. The background region was defined as an annulus centered on the source position, with an inner radius of 5° and an outer radius of 6° . In order to prevent contamination of the background sample from photons emitted by other astrophysical sources, all the sources in the 2FGL Catalog [13] were masked. Using

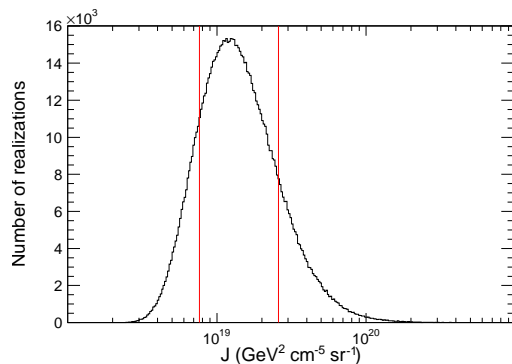


FIG. 1: Distribution of 10^6 J -factor values for the stacked sources. Each realization is obtained by sampling the 10 log-normal distributions of the J -factors of individual sources and evaluating the average value weighted by the exposures. The red lines correspond to the 16% and 84% quantiles of the distribution.

the HEALPix [21] pixelization scheme with $N_{\text{side}} = 256$, the sky was divided into 786432 equal area pixels, each covering a solid angle of $1.6 \cdot 10^{-5}$ sr. The background region was composed of all the pixels in the annulus, excluding those at an angular distance less than 3° from any point source and those at an angular distance less than 3° plus the angular size of the semi-major axis from any extended source. The solid angle of the background region, $\Delta\Omega_{bi}$, was then evaluated by adding the solid angles corresponding to all the unmasked pixels in the annulus.

Fig. 2 shows the photon count maps with energy greater than 562 MeV for the 10 dSph galaxies considered in the present analysis. A qualitative inspection of the count maps shows no evidence of a gamma-ray signal from any dSph galaxy. On the other hand, from Fig. 2, bright gamma-ray sources close to some dSph galaxies are evident. However, as mentioned above, these sources are not considered when evaluating the background because of the masking procedure.

Photons emitted by possible gamma-ray point sources lying close to a dSph galaxy might be detected in the signal region. These photons will not be accounted for in the background and, therefore, they might be confused with a DM annihilation signal. The result is that the upper limits on the DM signal will be higher and so, in this sense, this analysis is conservative.

Fig. 3 shows the signal and background count distributions for all the dSph galaxies that were analyzed. The background counts have been scaled taking into account the solid angle ratio between the signal and background regions, according to Eq. 5 (Eq. 11 in the case of the stacking analysis). In all cases no evidence is observed of a net signal excess with respect to the background in any energy bin.

Fig. 4 shows the upper limits at 95% CL on the flux (top panel) and on $\Phi^{PP}(E)$ (bottom panel) as function of the energy, for each of the dSph galaxies considered in this analysis. The more constraining limits are those obtained from the dSph galaxies with the highest J -factors.

Once the individual sources were analyzed, the stacking analysis and the composite analysis were implemented following the procedures described in §III B and in §III C. As mentioned above, for the stacking analysis the counts from the signal and background regions corresponding to each source were added, and the upper limits on the signal were evaluated following the same procedure as for individual sources. This approach is equivalent to stacking the events from all the dSph galaxies and then analyzing the single image obtained from the superposition of all the individual images (see the last plots in Figs. 2 and 3).

It is worth noting that in the high-energy bands, where the counts in the signal and background regions are both null (i.e. $n = m = 0$), as shown in Fig. 3, the upper limit evaluated on the signal counts is always constant (i.e., at 95% CL the upper limits on s corresponds to

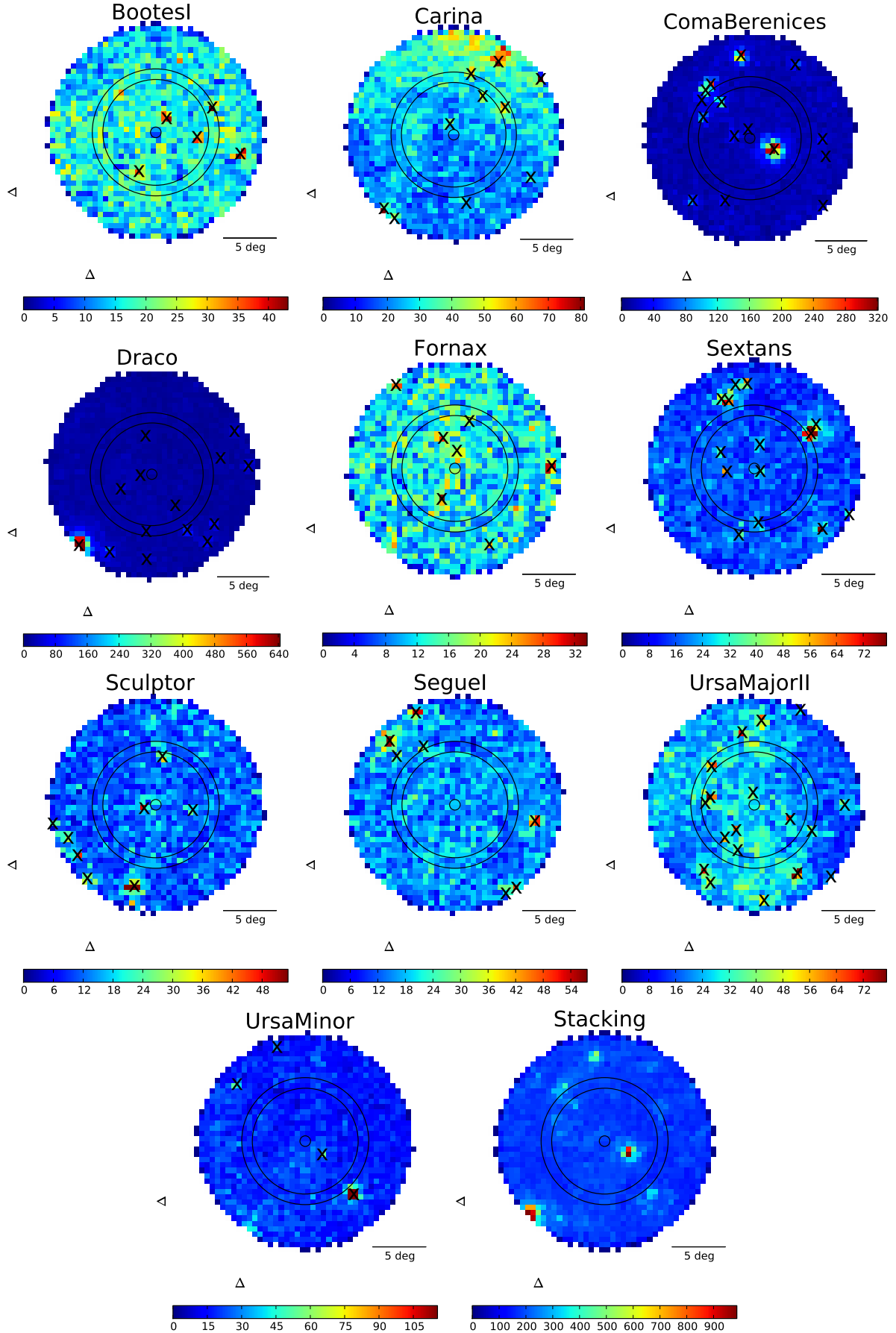


FIG. 2: Photon count maps in the observed energy range from 562 MeV to 562 GeV for the dSph galaxies considered in this analysis. The black circles indicate the cones of angular radii of 0.5° , 5° and 6° , representing the boundaries of the signal and background regions. The sources in the 2FGL Catalog are indicated with crosses. Each map is centered on the position of the corresponding source. The map in the bottom right panel was obtained by stacking the data from all the dSph galaxies.

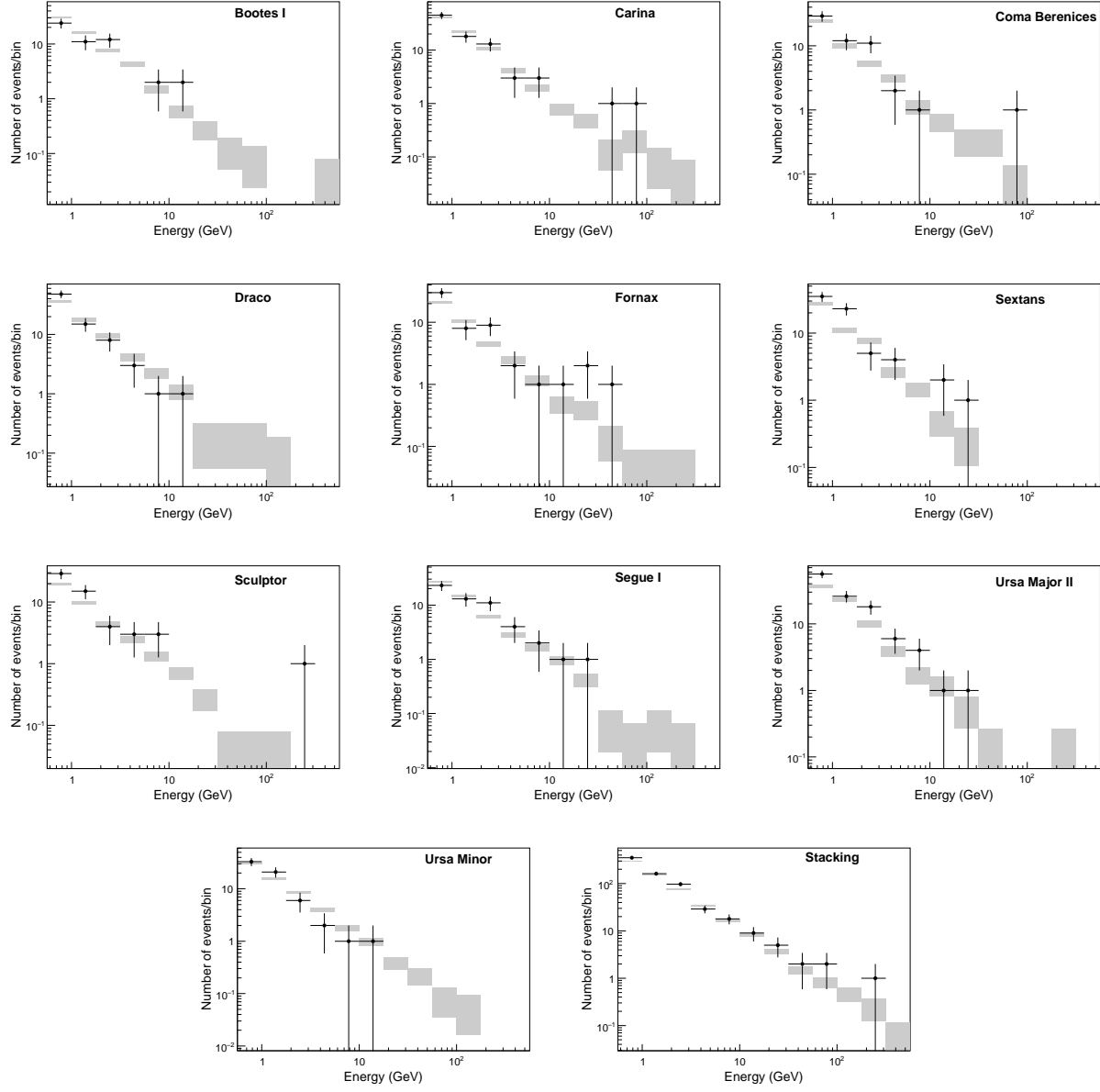


FIG. 3: Count distributions in the observed energy range from 562 MeV to 562 GeV for the dSph galaxies considered in this analysis. The black points represent the counts in the signal region; the grey areas represent the equivalent number of background counts (i.e., the counts in the background region scaled by the coefficient c) with their errors. The bottom right panel shows the distribution obtained by stacking all the dSph galaxies.

about 3 counts). Hence, when performing the stacking analysis, the upper limit on the flux (see top panel of Fig. 4) will decrease linearly with the number of stacked sources. In other words, in the stacking analysis the observations of different sources are added and the result is expected to be equivalent to a single observation of an individual source with a total live time corresponding to the sum of the live times of each observation. On the other hand, in the low-energy band, where the counts in the signal region are roughly equal to those in the background region (i.e. $n \approx c m$), the upper limit on the signal counts s is roughly proportional to the square root of the observed events [15]. In this case, since the total live time will be roughly proportional to the number of

stacked sources, the upper limit on the stacked flux will improve with the square root of the number of stacked sources.

In the bottom panel of Fig. 4 the upper limits on $\Phi_{PP}(E)$ are shown for all the candidate sources as well as for the stacking and composite analyses. As shown in Tab. I, the J -factors of the 10 dSph galaxies studied in the present analysis are distributed in an interval that spans two orders of magnitude. As a consequence, since the upper limits on the photon fluxes are roughly similar, the upper limits on $\Phi^{PP}(E)$ will span two orders of magnitude. The stacking analysis improves the upper limits on $\Phi^{PP}(E)$ by a factor that ranges from a few to about 10 with respect to those obtained from the analysis of individual dSph galaxies. When considering the quantity $\Phi^{PP}(E)$, since the J -factor used in the stacking analysis is evaluated as the average of the J -factors of individual sources weighted with their exposures, the result is an improvement of a factor of a few with respect to the upper limits obtained from the analysis of the source with the highest J -factor.

The results from the composite analysis are in general more constraining than those from the stacking analysis. This could be due to the fact that the random variable used to evaluate the upper limits in the composite analysis is $\propto \prod_i s_i/J_i$, while the random variable used in the stacking analysis is $\propto (\sum_i s_i)/\langle J \rangle$. This means that the “effective J -factor” for the composite analysis could in principle be different from that for the stacking analysis.

The measured upper limits on $\Phi^{PP}(E)$ were converted into upper limits on $\langle \sigma v \rangle$ following the procedure described in §III A. Fig. 5 shows an example of this calculation in the case of Segue I for the annihilation channels $\mu^+\mu^-$, $\tau^+\tau^-$, $b\bar{b}$ and W^+W^- . The upper limits were also evaluated taking into account separately the uncertainties on the effective area and on the J -factors. To describe the systematic uncertainties on the effective area we assumed a uniform PDF centered on the average value $A(E)$ in each energy bin with fluctuations of $\pm 10\%$. These uncertainties have a negligible effect on the upper limits. As discussed above, the effects on the upper limits due to the systematic uncertainties on the J -factor were evaluated assuming for J a uniform PDF in a range corresponding to the 68% area of the actual J -factor distribution. As shown in Fig. 5, the effects of the uncertainties on the J -factor are not negligible and, depending on the source under investigation, the upper limits on $\Phi^{PP}(E)$ can increase by up to a factor of a few.

Fig. 6 shows the upper limits at 95% CL on $\langle \sigma v \rangle$ obtained from the analysis of individual dSph galaxies, from the stacking analysis and from the composite analysis, as a function of the WIMP mass for the annihilation channels $\mu^+\mu^-$, $\tau^+\tau^-$, $b\bar{b}$ and W^+W^- . The upper limits obtained by taking into account the effects of the uncertainties on the J -factors are also shown.

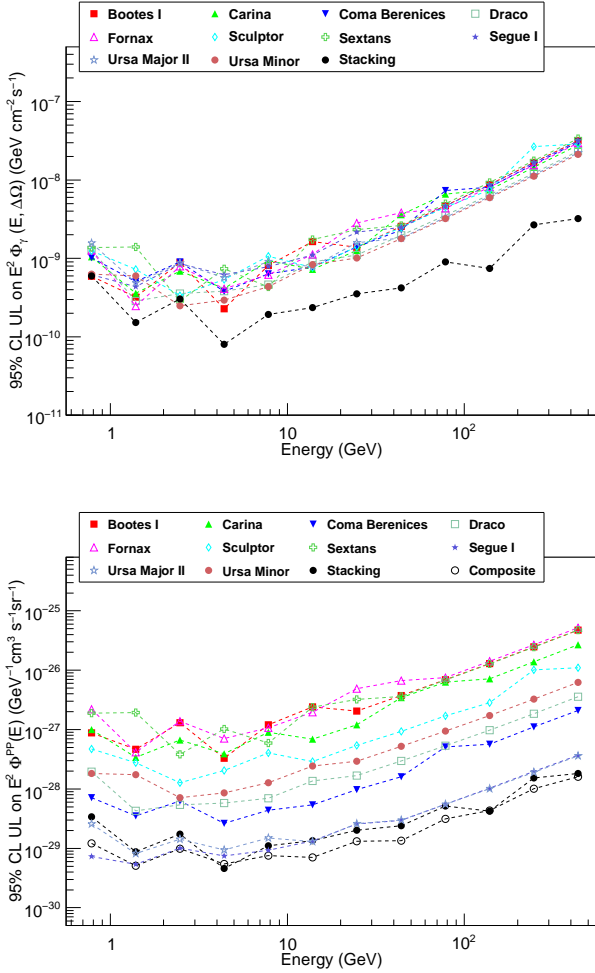


FIG. 4: Top panel: Upper limits at 95% CL on the gamma-ray flux as function of energy. Bottom panel: Upper limits at 95% CL on $\Phi^{PP}(E)$ as function of energy. The colored symbols correspond to the results obtained from the individual dSph galaxies. The open black circles indicate the results obtained from the composite analysis, while the filled black circles indicate the results obtained from the stacking analysis of all the dSph galaxies.

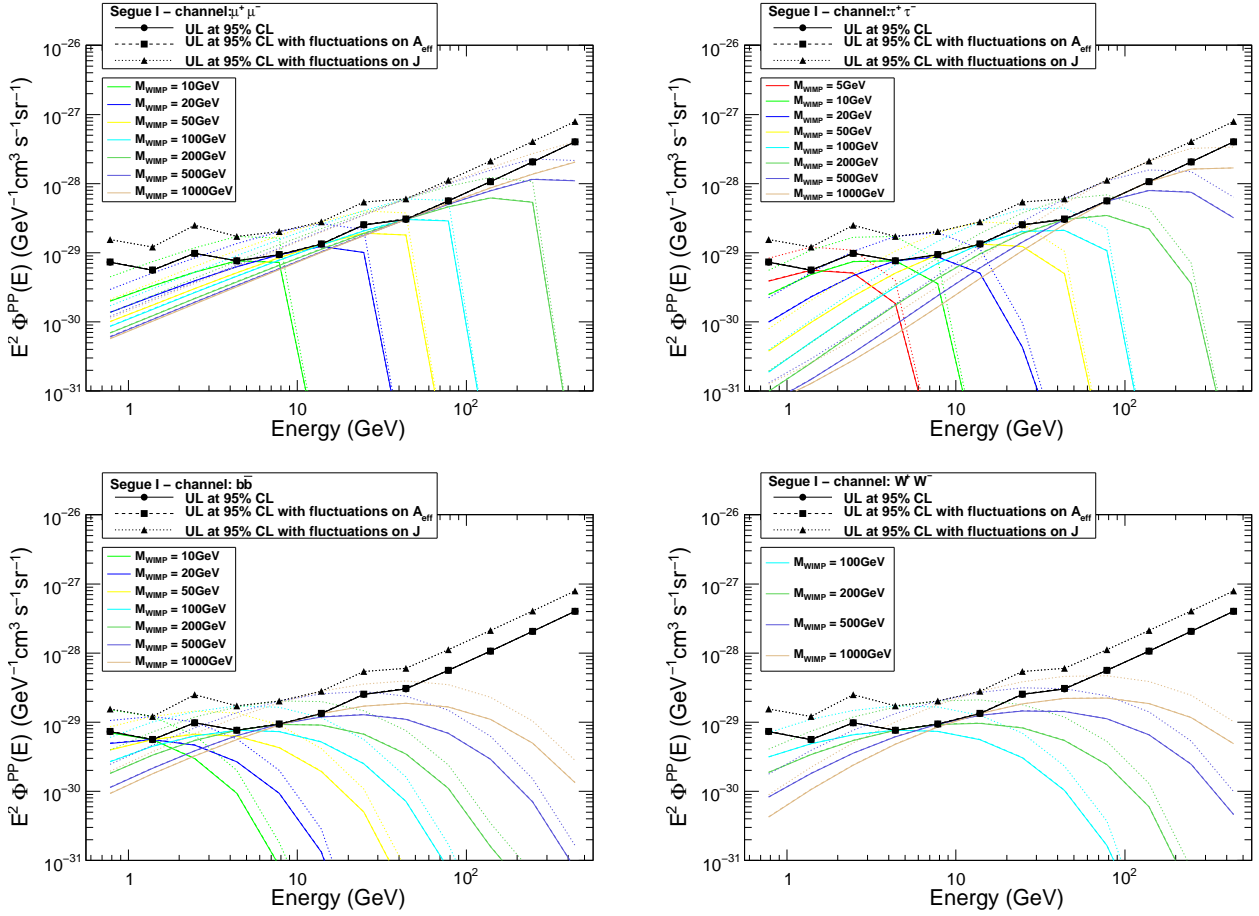


FIG. 5: Evaluation of the upper limits on $\langle\sigma v\rangle$ as a function of the true energy for several WIMP mass values in the case of Segue I. The black lines with full circles correspond to the upper limits at 95% CL on $\Phi^{PP}(E)$. The colored lines, each corresponding to a specified WIMP mass, indicate the maximum allowed values of $\Phi^{PP}(E)$ that do not exceed the measured upper limits. The four panels refer to WIMP annihilation into $\mu^+\mu^-$, $\tau^+\tau^-$, $b\bar{b}$ and W^+W^- (as labeled). The dashed lines with filled squares and the dotted lines with filled triangles indicate the upper limits evaluated taking into account the systematic uncertainties on the effective area and on the J-factors, respectively. The effects of the systematic uncertainties on the effective area are negligible (dashed lines and filled squares are almost coincident with continuous lines and filled circles).

V. ANALYSIS OF THE MILKY WAY HALO

The study of the Milky Way halo is quite complex because its gamma-ray emission has to be disentangled from that of known gamma-ray sources. However, a possible approach to the study of the Milky Way halo is that of selecting a set of sky directions that are well-separated from known gamma-ray sources.

For this analysis a set of 1000 random directions was generated in the sky, each direction located at an angular distance of at least 3° from all the 1873 point sources and at least 3° plus twice the size of the semi-major axis from all the 11 extended sources in the 2FGL Catalog [13]. The random positions are illustrated in Fig. 7 in Galactic coordinates. Since many gamma-ray sources are concentrated in the region of the Galactic plane, we also decided to perform a separate analysis selecting only random directions at an angular distance

larger than 10° from the Galactic plane (i.e. all directions with Galactic latitude $|\beta| > 10^\circ$). A subset of the initial sample, consisting of 866 random directions, was used for this analysis.

The analysis of the Milky Way Halo was performed selecting P7CLEAN_V6 class events in order to guarantee optimal rejection of the charged particle background. As in the case of the dSph galaxies, discussed in §IV, the data analysis was performed selecting gamma rays with energies from 562 MeV to 562 GeV, with the energy interval being divided into 12 bins, equally spaced on a logarithmic scale.

In the case of the Galactic halo analysis, we hypothesized an extreme scenario in which all the detected photons originate from DM annihilation. In this analysis the upper limits on $\Phi^{PP}(E)$, and consequently those on $\langle\sigma v\rangle$, were evaluated assuming an absence of background events. For each random direction the signal

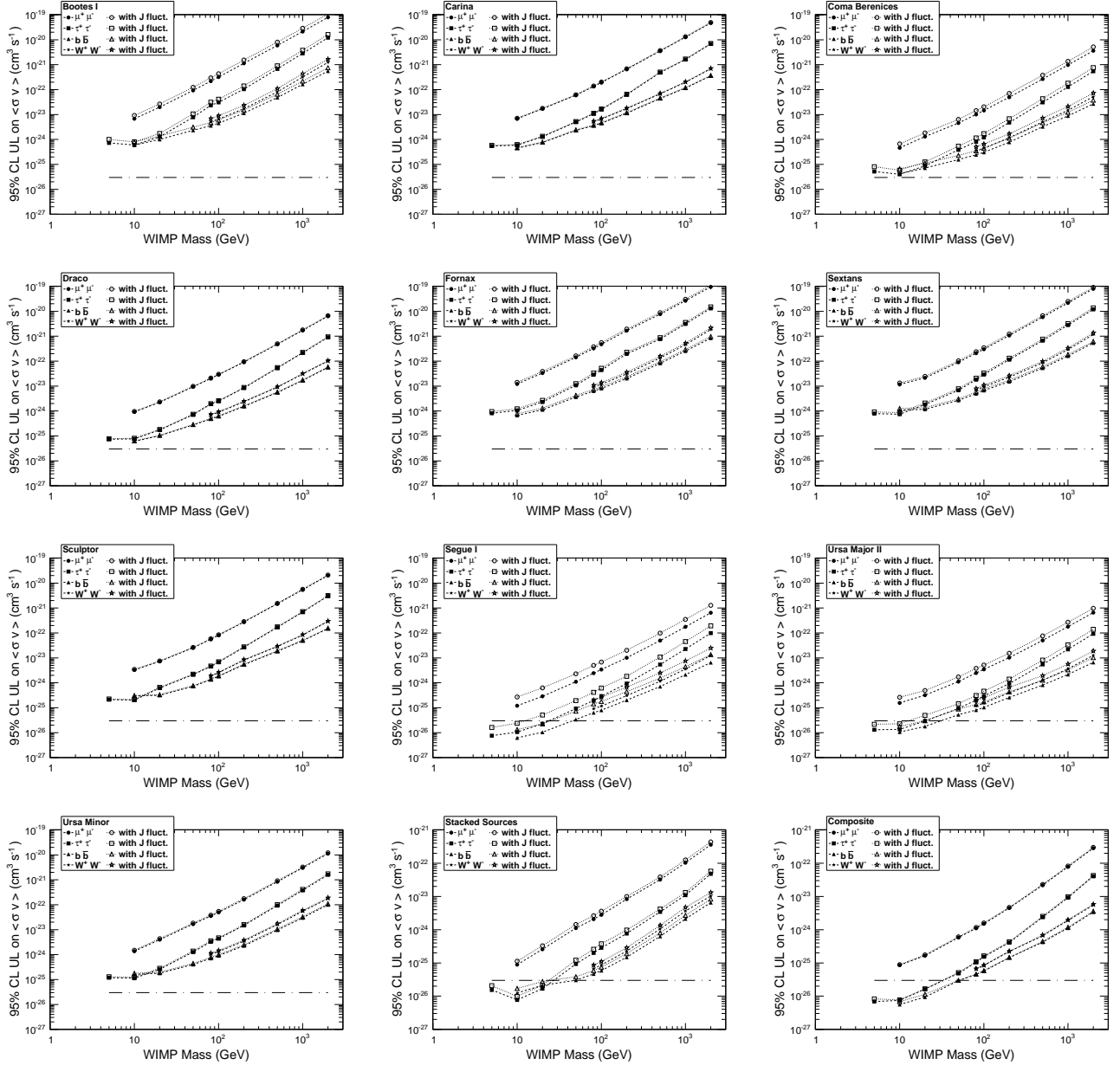


FIG. 6: Upper limits at 95% CL on $\langle\sigma v\rangle$ as function of the WIMP mass for the annihilation channels $\mu^+\mu^-$, $\tau^+\tau^-$, $b\bar{b}$ and W^+W^- . The plots show the upper limits obtained from the analysis of individual dSph galaxies and from the stacking and composite analyses. The continuous lines indicate the upper limits obtained neglecting the systematic uncertainties, while the dotted lines indicate the upper limits obtained including the uncertainties on the J -factors. The long dashed line corresponds to the canonical value of the annihilation cross section of $3 \times 10^{-26} \text{ cm}^3 \text{s}^{-1}$ in the thermal relic WIMP scenario.

region was defined as a cone of angular radius $\Delta\theta = 1^\circ$ centered on it. The analysis was then performed stacking the data from all the random directions, without background subtraction (i.e. $c = 0$ and $m = 0$). This strategy relies on the assumption that a possible DM-induced gamma-ray flux must be lower than the total observed flux. The upper limits obtained from this analysis therefore will be conservative.

For any given random direction (hereafter we will refer to random directions as sources) the J -factor was

evaluated using Eq. 2. Since the signal region is a narrow cone of 1° angular radius, Eq. 2 reduces to:

$$J \approx \Delta\Omega \int \rho^2(l(\psi)) dl. \quad (34)$$

where $\Delta\Omega \approx 9.6 \cdot 10^{-4} \text{ sr}$ is the solid angle corresponding to the signal region. In the previous equation we explicitly wrote the dependence of the DM density on the angle ψ , which represents the angular separation of

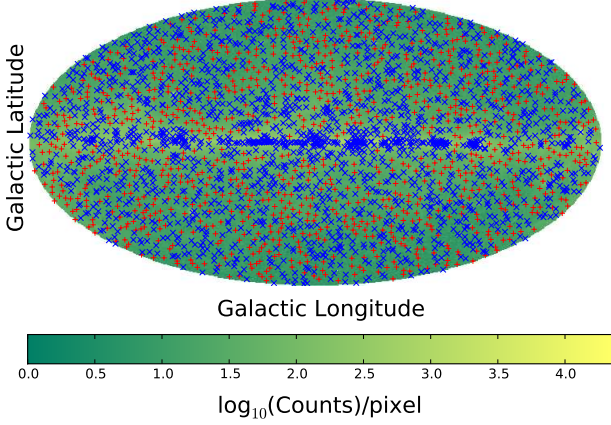


FIG. 7: Count map used for the analysis of the Milky Way Halo. The map was built in the Galactic reference frame, using the HEALPix pixelization scheme with $N_{\text{side}} = 128$ (196608 pixels, each covering a solid angle of $6.4 \cdot 10^{-5}$ sr), and is displayed in the Aitoff projection. The Galactic Center is in the middle of the map. The 1000 random directions are indicated with the red markers; the sources in the 2FGL Catalog are indicated with the blue markers.

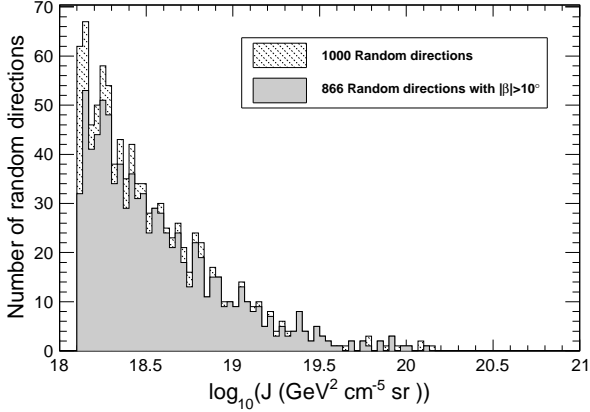


FIG. 8: Distribution of the J -factors evaluated for the random directions in the Galactic halo. The dashed filled region shows the J -factors of all the 1000 directions; the grey filled region shows the J -factors for the 866 sky directions that are separated more than 10° from the Galactic plane.

the source from the Galactic Center.

In performing the calculations we assumed that the detector is located at the Sun's position and we used the Galactic reference frame. The angle ψ can then be calculated from the Galactic longitude and latitude (λ, β) using the following relation:

$$\cos \psi = \cos \lambda \cos \beta. \quad (35)$$

For the DM density we assumed a Navarro-Frenk-White (NFW) profile [22]:

$$\rho(r) = \frac{\rho_0}{(r/r_s)(1 + r/r_s)^2} \quad (36)$$

where $\rho_0 = 0.3 \text{ GeV/cm}^3$ and $r_s = 20 \text{ kpc}$. The coordinate r in Eq. 36 represents the distance from the Galactic Center, and is given by:

$$r = \sqrt{l^2 + R_0^2 - 2lR_0 \cos \psi} \quad (37)$$

where $R_0 = 8.5 \text{ kpc}$ is the distance of the Galactic Center from the Sun and l is the distance of the line element dl from the Sun.

Fig. 8 shows the distribution of the J -factors evaluated for the sky directions shown in Fig. 7. As expected, the directions with the highest J -factors are near the Galactic Center; on the other hand, the directions with the lowest J -factors are near the Galactic Anti-center.

The stacking analysis was performed as described in §III B. In our model we assumed that all photons originate from DM, and the upper limits on the signal counts were evaluated using the PDF in Eq. 8. We also performed the composite analysis of the random sources following the procedure described in §III C, and in this

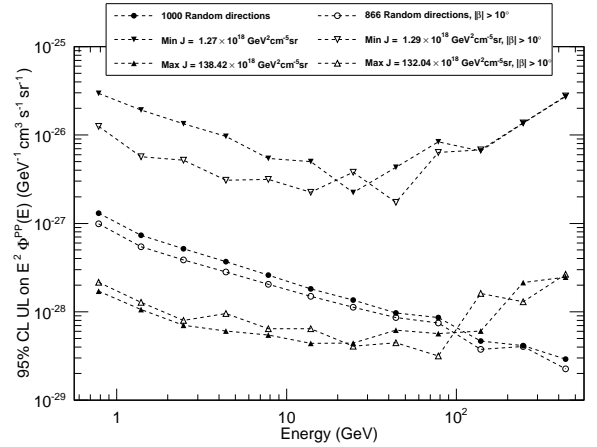


FIG. 9: Comparison of the 95% CL upper limits on $\Phi^{PP}(E)$ as function of the energy for all of the 1000 random directions and for the 866 directions outside the Galactic plane ($|\beta| > 10^\circ$). The upper limits obtained from the directions corresponding to the highest and lowest J -factors are also shown. The lowest J -factor among the 1000 sky directions is associated with the direction (in Galactic coordinates) $(\lambda, \beta) = (183.616^\circ, -0.189^\circ)$, while the highest J -factor is associated with the direction $(356.796^\circ, 9.23^\circ)$. The lowest J -factor among the 866 sky directions outside the Galactic plane is associated with the direction $(179.968^\circ, -11.5651^\circ)$, while the highest J -factor is associated with the direction $(0.621474^\circ, 10.0793^\circ)$.

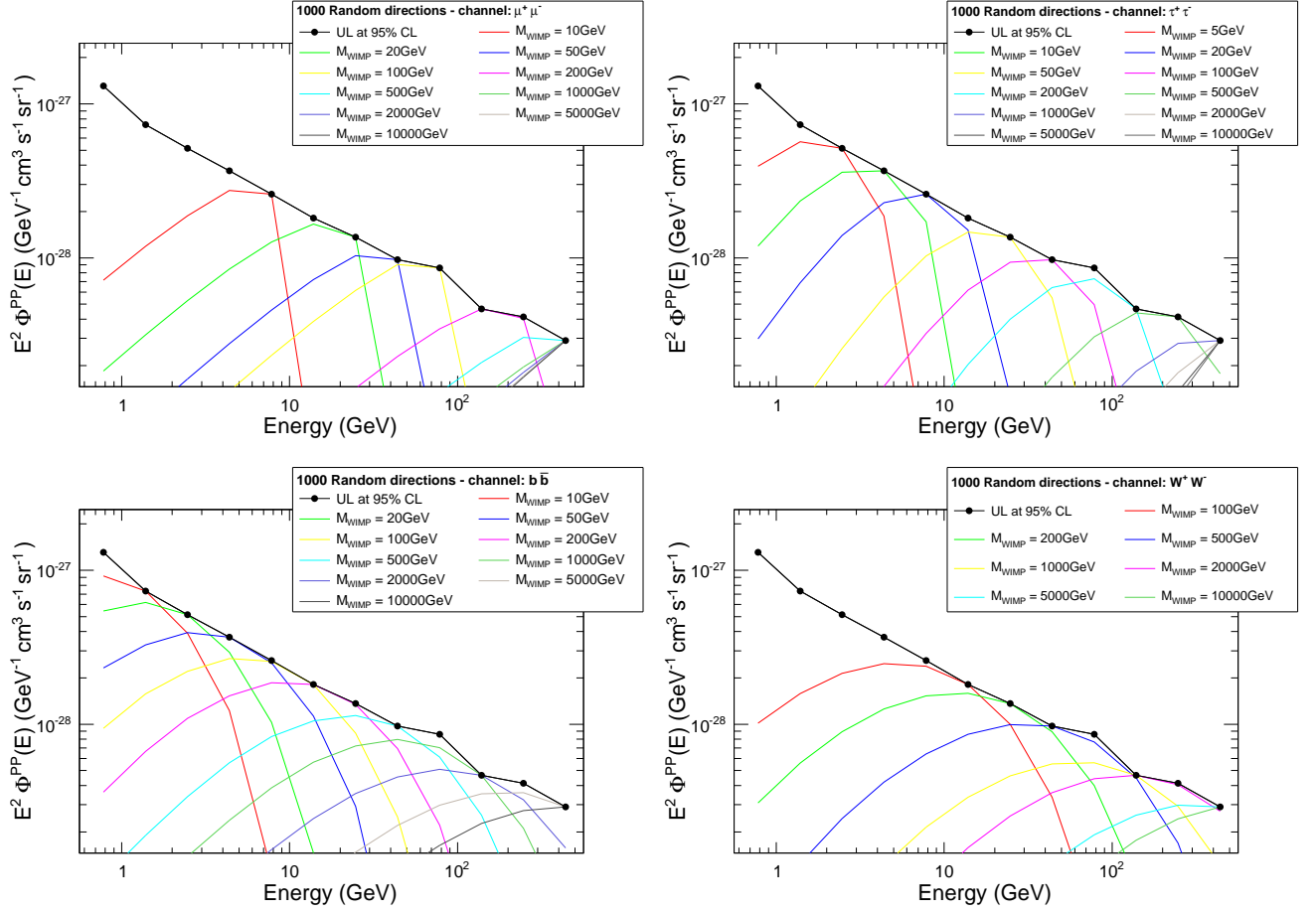


FIG. 10: Evaluation of the upper limits on $\langle\sigma v\rangle$ as a function of the true energy for several WIMP mass values from the Galactic halo analysis with the stacking of all the 1000 random directions. The black lines correspond to the upper limits at 95% CL on $\Phi^{PP}(E)$. The colored lines, each corresponding to a given value of the WIMP mass, indicate the maximum allowed values of $\Phi^{PP}(E)$ that do not exceed the measured upper limits. The four panels refer to the WIMP annihilations into $\mu^+\mu^-$, $\tau^+\tau^-$, $b\bar{b}$ and W^+W^- , respectively, as labeled.

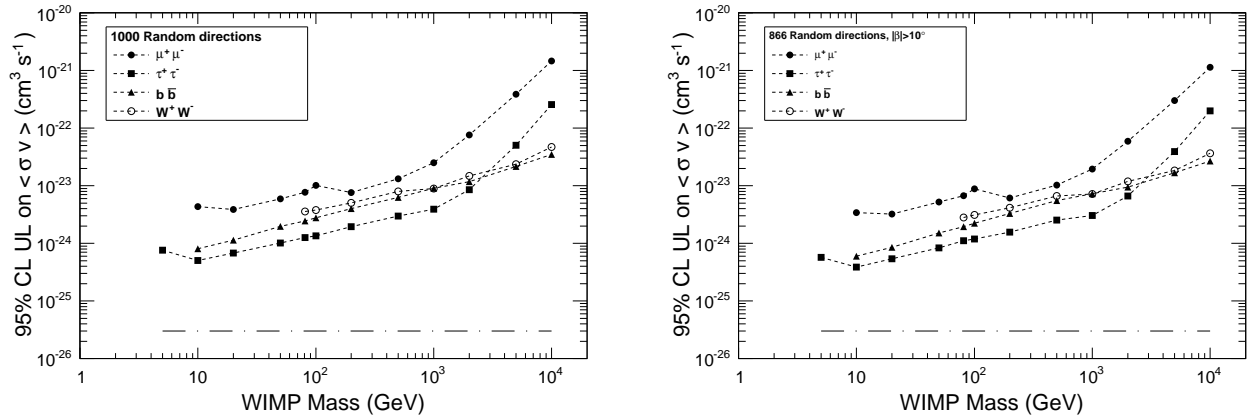


FIG. 11: Upper limits at 95% CL on $\langle\sigma v\rangle$ as a function of the WIMP mass for the annihilation channels $\mu^+\mu^-$, $\tau^+\tau^-$, $b\bar{b}$ and W^+W^- . The plot shows the results obtained from the analyses of the Milky Way halo with all the 1000 directions (left panel) and with the 866 directions with $|\beta| > 10^\circ$ (right panel). The dashed line is the annihilation cross section of $3 \times 10^{-26} \text{cm}^3 \text{s}^{-1}$ in the canonical thermal relic WIMP scenario.

case the results were equivalent to those obtained from the stacking analysis.

Fig. 9 shows the upper limits at 95% CL on $\Phi^{PP}(E)$ for the Milky Way halo evaluated using all the 1000 random directions and only the 866 directions with $|\beta| > 10^\circ$. The upper limits obtained from the directions with the lowest and the highest J -factors are also shown. The directions with the highest J -factor yield the more constraining upper limits on $\Phi^{PP}(E)$. This result is not completely obvious, since the directions with the higher J -factors are in the region of the Galactic Center, where a high number of photons is expected, while the directions with the lower J -factors are in the region of the Galactic Anti-center, where a lower number of photons is expected. The upper limits obtained from the analysis of the direction with the highest J -factor are also more constraining than the ones from the stacking analysis, with the exception of the high energy regime, where the constraints from the stacking analysis are tighter. This is due to the fact that in the high-energy regime the number of events in the signal regions is low, and consequently the upper limits on the fluxes decrease with increasing live time.

Fig. 10 shows the procedure used to convert the measured upper limits on $\Phi^{PP}(E)$ into upper limits on $\langle\sigma v\rangle$ in the case of the stacking analysis of all the 1000 random sources. As in the case of the dSph analysis, we imposed the requirement that the flux values predicted from the DM annihilation scenarios must not exceed the measured upper limits in any energy bin.

In Fig. 11 the upper limits at 95% CL on $\langle\sigma v\rangle$ as a function of the WIMP mass are shown for WIMP annihilations into $\mu^+\mu^-$, $\tau^+\tau^-$, $b\bar{b}$ and W^+W^- for the Milky Way halo. These results have been obtained from the analysis of all the 1000 random directions (left plot) and from the analysis of the 866 directions with $|\beta| > 10^\circ$ (right plot) (see Fig. 9). If only the direction with the highest J -factor were analyzed, the upper limits on $\langle\sigma v\rangle$ in the low WIMP-mass regime would be about a factor 10 more constraining than those obtained from the combined analyses.

VI. DISCUSSION

In this work we used the gamma-ray data collected by the Fermi LAT during its first 3 years of operation to set constraints on the parameter $\langle\sigma v\rangle$ assuming DM annihilation into various channels.

We studied a set of 10 Milky Way dSph satellite galaxies and the Milky Way halo. The dSph galaxies were analyzed both individually and collectively, implementing dedicated stacking and composite analysis procedures. The Milky Way halo was studied by randomly sampling a set of 1000 sky directions well-separated from all the gamma-ray sources of the 2FGL Catalog and performing a stacking analysis. The data analysis was performed using a model-independent

method that allows upper limits to be set on the gamma-ray fluxes starting from the observed events using a Bayesian approach. The constraints on $\langle\sigma v\rangle$ were derived requiring that the predicted fluxes from the models must not exceed the measured ones.

The analysis of the dSph galaxies yields upper limits on $\langle\sigma v\rangle$ that are lower with respect to the predictions from a canonical thermal WIMP scenario for the $\tau^+\tau^-$ and $b\bar{b}$ final states up to masses of few tens of GeV. This is found in the stacking and in the composite analysis results, but also in the results of the individual analyses of the dSph galaxies with the highest J -factors. The uncertainties in the J -factor calculation and on the effective area of the LAT were also included in the present analysis, and do not affect significantly the upper limits. Our results are consistent with recent analyses [5, 6] performed using different approaches. However, we emphasize that the upper limits on the parameter $\langle\sigma v\rangle$ depend strongly on the values of the J -factor. In particular, since no evidence of a gamma-ray flux is observed from any dSph galaxy, the upper limits on $\Phi^{PP}(E)$ and consequently those on $\langle\sigma v\rangle$ will scale with the J -factor (see Fig. 4).

For comparison, the analysis of the dSph galaxies was also performed using the P6_V3_DIFFUSE IRFs, as were used in Ref. [5], and the results were found to be in agreement with the ones already presented here, which were obtained using the P7SOURCE_V6 IRFs.

The analysis of the Milky Way halo, performed looking at a set of 1000 clean sky directions, yields upper limits on $\langle\sigma v\rangle$ that range from 10^{-25} to $10^{-23} \text{ cm}^3 \text{ s}^{-1}$ for WIMP masses below 10 TeV or more for the $b\bar{b}$ and W^+W^- annihilation channels. More constraining limits on $\langle\sigma v\rangle$ can be obtained in the low-energy region if the analysis is limited to the direction with the highest J -factor. These limits were evaluated assuming a NFW profile with a DM density at the solar circle of 0.3 GeV cm^{-3} , and their values depend on the DM mass density profile. A recent analysis suggested a revised value of the DM density at the solar circle of 0.43 GeV cm^{-3} [23]; under this assumption the upper limits on $\langle\sigma v\rangle$ would improve by a factor of 2. Nevertheless we note that the sky directions used for the present analysis are sufficiently far away from the Galactic Center that the J -factors evaluated with different DM density profiles would likely yield similar results (see Ref. [24]). The current results are consistent with the results obtained by Ref. [25], where an analysis of the all-sky Fermi LAT data was performed with a different model-independent technique. The Milky Way halo can also be studied following a different approach, in which a model is assumed for the Galactic diffuse gamma-ray emission and a fit of the DM signal together with the diffuse component is performed (e.g., see [26]). Our results are also consistent with those obtained from that analysis.

Both from the limits on the dSph galaxies (Fig. 6) and those on the Milky Way halo (Fig. 11), it is possible to restrict the range of allowed WIMP masses assuming

the standard thermal relic scenario. We also note that the DMFIT package may underestimate the gamma-ray fluxes for WIMP masses above 1 TeV, since it does not include radiative electroweak corrections; hence, the limits on $\langle\sigma v\rangle$ for large masses can be viewed as more conservative than those in the low mass region.

VII. CONCLUSIONS

We developed a model-independent approach to set upper limits on the energy spectra of both individual and multiple gamma-ray sources using the data collected by the Fermi LAT. In this paper we presented the results obtained from the application of this technique to the study of a set of dSph galaxies and to the study of the Milky Way halo. These results were used to derive constraints on DM annihilation cross sections into different channels. We emphasize that the analysis techniques presented in this paper are general, and are suitable for applications where the study of a class of sources, even faint sources, with common features have to be studied.

The data analysis technique illustrated in the present paper allows us to set robust upper limits on the energy spectra of candidate gamma-ray sources. The upper limits on the gamma-ray fluxes are in fact derived starting from the data, without assuming any model for the background and for the source spectral shapes. The signal is evaluated selecting events from a cone centered on the source position, while the background is evaluated selecting events in a region close to the source under investigation. Both signal and background fluctuations are described in the framework of Poisson statistics, and the upper limits on the signal counts, and consequently on the flux, are computed following the Bayesian approach. A stacking analysis and a composite analysis procedure have also been developed to perform the collective study of multiple candidate sources with common features.

The analysis methods presented in this paper can also be applied when several measurements of a given physical quantity, each one resulting into a confidence interval, have to be combined into a unique confidence interval taking all the results into account. The systematic uncertainties can also be incorporated in the analysis by introducing proper nuisance parameters in the probability distribution functions.

Acknowledgements

The Fermi LAT Collaboration acknowledges generous ongoing support from a number of agencies and institutes that have supported both the development and the operation of the LAT as well as scientific data analysis. These include the National Aeronautics and Space Administration and the Department of Energy in the

United States, the Commissariat à l’Energie Atomique and the Centre National de la Recherche Scientifique / Institut National de Physique Nucléaire et de Physique des Particules in France, the Agenzia Spaziale Italiana and the Istituto Nazionale di Fisica Nucleare in Italy, the Ministry of Education, Culture, Sports, Science and Technology (MEXT), High Energy Accelerator Research Organization (KEK) and Japan Aerospace Exploration Agency (JAXA) in Japan, and the K. A. Wallenberg Foundation, the Swedish Research Council and the Swedish National Space Board in Sweden.

Additional support for science analysis during the operations phase is gratefully acknowledged from the Istituto Nazionale di Astrofisica in Italy and the Centre National d’Études Spatiales in France.

Some of the results in this paper have been derived using the HEALPix package [21].

The authors thank James Chiang and Jennifer Siegal-Gaskins for their valuable contributions during the preparation of the manuscript.

Appendix A: Derivation of Equation 12

When performing the stacking analysis of a set of multiple sources, the counts from the individual signal and background regions are added. The total counts in the signal and background region are then given by:

$$n = \sum_i n_i \quad (\text{A1})$$

$$m = \sum_i m_i \quad (\text{A2})$$

where n_i and m_i are respectively the counts in the signal and in the background region of the i -th source.

According to the assumptions in §III A, n_i and m_i are both Poissonian with expectation values $s_i + c_i b_i$ and b_i (in the following we shall use the notation $n_i \sim \mathcal{P}(s_i + c_i b_i)$ and $m_i \sim \mathcal{P}(b_i)$). Hence, from the definitions of n and m it follows that:

$$n \sim \mathcal{P}\left(\sum_i (s_i + c_i b_i)\right) \quad (\text{A3})$$

$$m \sim \mathcal{P}\left(\sum_i b_i\right). \quad (\text{A4})$$

In the stacking analysis the true values of the signal and of the background counts are defined as:

$$s = \sum_i s_i \quad (\text{A5})$$

$$b = \sum_i b_i. \quad (\text{A6})$$

This definition automatically implies that $m \sim \mathcal{P}(b)$. However, to ensure that $n \sim \mathcal{P}(s + cb)$, the coefficient c must be defined as:

$$c = \frac{\sum_i c_i b_i}{\sum_i b_i}. \quad (\text{A7})$$

The values of b_i are not known, but they can be replaced with their best estimators $b_i^* = m_i + 1$ [27]. In this way, Eq. A7 reduces to Eq. 12.

-
- [1] J. Wolf, G.D. Martinez, J.S. Bullock, J. S. et al., MNRAS 406 (2010) 1220
 - [2] J.D. Simon, M. Geha, Q.E. Minor et al., Astrophys. J. 733 (2011) 46
 - [3] E. Komatsu et al., ApJS 192 (2011) 18 arXiv:1101.4538
 - [4] A. Charbonnier et al., MNRAS (2011), arXiv:1104.0412
 - [5] M. Ackermann et al., (The Fermi LAT Collaboration), Phys. Rev. Lett. 107 (2011) 241302, arXiv:1108.3546
 - [6] A. Geringer-Sameth and S.M. Koushiappas Phys. Rev. Lett. 107 (2011) 241303, arXiv:1108.2914
 - [7] G. Jungman, Kamionkowski and Greist, Phys. Rep. 267 (1996) 195
 - [8] F. de Palma, F. Loparco and M.N. Mazziotta Contribution to the Fermi Symposium 2011 <https://confluence.slac.stanford.edu/download/attachment/102860834/DMNP51n89.pdf>
 - [9] M.N. Mazziotta, contribution to 31st ICRC , arXiv 0912.1236
 - [10] F. Loparco and M.N. Mazziotta, Contribution to the II Fermi Symposium, arXiv 0912.3695
 - [11] A.A. Abdo et al. (The Fermi LAT Collaboration), Astrophys. J. 716 (2010) 30
 - [12] W.B. Atwood et al. (The Fermi LAT Collaboration), Astrophys. J. 697 (2009) 1071
 - [13] A.A. Abdo et al. (The Fermi LAT Collaboration) 2nd Fermi LAT Catalog 2011, arXiv:1108.1435, http://fermi.gsfc.nasa.gov/ssc/data/access/lat/2yr_catalog/, version: gll_psc_v06.fit
 - [14] http://www.slac.stanford.edu/exp/glast/groups/canda/lat_Per
<http://fermi.gsfc.nasa.gov/ssc/data/analysis/documentation/>
 - [15] F. Loparco and M.N. Mazziotta, Nucl. Inst. Meth. A646 (2011), 167-173
 - [16] T.E. Jeltema and S. Profumo, J. Cosmol. Astropart. Phys., 0811 (2008) 003
 - [17] P. Gondolo et al., J. Cosmol. Astropart. Phys., 0407 (2004) 008
 - [18] <http://fermi.gsfc.nasa.gov/ssc/data/analysis/documentation/>
 - [19] N. F. Bell et al., Phys. Rev. D78 (2008) 083540
 - [20] P. Ciafaloni et al., J. Cosmol. Astropart. Phys. 03 (2011) 019
 - [21] K.M. Gorski, E. Hivon, A.J. Banday *et al.*, Astrophys. J. 622 (2005) 759, astro-ph/0409513, <http://arxiv.org/abs/astro-ph/0409513>
 - [22] J.F. Navarro et al., Astrophys. J. 490 (1997), 493
 - [23] P. Salucci, F. Nesti, G. Gentile and C. Frigerio Martins, Astron. Astrophys. 523 (2010) A83, arXiv:1003.3101
 - [24] L. Bergströma, P. Ullio and J. H. Buckley, Astroparticle Physics 9 (1998) 137
 - [25] M. Papucci and A. Strumia, J. Cosmol. Astropart. Phys. 1003 (2010) 014, arXiv:0912.0742
 - [26] G. Zaharijas, A. Cuoco, Z. Yang, J. Conrad (for the Fermi-LAT collaboration), arXiv:1012.0588
 - [27] G. D'Agostini, Rep. Prog. Phys. 66 (2003) 1383